IJSCIA

International Journal of Scientific Advances
ISSN: 2708-7972
Volume: 7 | Issue: 6 | Nov – Dec 2026 Available Online: www.ijscia.com
DOI: 10.51542/ijscia.v7i6.4

Angle-Estimation Bias and Coupling-Model Accuracy Requirements for Mutual-Coupling Compensation in 77 GHz Automotive Radar: A Simulation Study

Md Nadim Hosain[1], Anup Chandra Sagor[2], Md Emadur Rahman Ekra[1*], Ashikur Mollik[1]

[1]School of Electronics and Information Engineering,
Nanjing University of Information Science and Technology, Nanjing, China

[2]School of Computer Science and Technology,
Nanjing University of Information Science and Technology, Nanjing, China

E-mail: mdnadimhosain@nuist.edu.cn; mdemandekra@nuist.edu.cn;
anupchandrasagor@nuist.edu.cn; ashikurmollik@nuist.edu.cn

*Corresponding author details: Md Emadur Rahman Ekra; mdemandekra@nuist.edu.cn

ABSTRACT

Mutual coupling between closely spaced receive elements biases angle-of-arrival (AoA) estimates in automotive radar, and digital compensation removes this bias only if the assumed coupling matrix is accurate. In this study, we quantify how accurate it must be. We model an eight-element, half-wavelength patch array on Rogers RO3003 inside a complete 77 GHz FMCW chain (1 GHz chirp, 512 × 128 data cube, CA-CFAR) and compare conventional beamforming with inverse-matrix decoupling and a normalized coupled-manifold beamformer. Coupling is represented by a reduced banded model (−12 dB adjacent coupling) and, as a network-consistent benchmark, by impedance-derived coupling of half-wavelength dipoles. We show analytically that the bias equals the amplitude-weighted least-squares slope of the excess element phase; this predictor matches exact estimates within 0.004°. Without compensation, the bias reaches 0.97°, or 0.45 m of lateral error at 28.5 m, and dominates the error because the per-channel SNR after integration exceeds 20 dB for vehicle-sized targets. With an exact matrix, both estimators remove the bias, follow the Cramér–Rao bound, and cost under 0.3 dB of SNR. With an inexact matrix, the residual bias grows linearly with the coupling error: a 20% magnitude error leaves 9–19% of the bias, and a 10° phase error leaves 10–51%, depending on the coupling phase. A three-parameter banded fit fails on the network-consistent benchmark (1.99° of 2.23° remains), whereas a Toeplitz fit leaves 0.15°. Calibrating a Toeplitz-structured response from 13 angles holds the 95th-percentile residual below 0.2° at about 31 dB calibration SNR. All results are simulation-based; full-wave extraction and measurement remain necessary.

Keywords: automotive radar; FMCW radar; 77 GHz; array calibration; Cramér-Rao bound

INTRODUCTION

Automotive radar resolves targets in range and velocity with a bandwidth and a frame time that current 76–81 GHz transceivers provide comfortably; angle is harder, because it depends on the aperture and on how well the processor knows the response of every receive channel [1], [2]. A half-wavelength receive array at 77 GHz fits in about 14 mm, so its elements couple strongly: each element re-radiates part of the incident field, and the embedded element patterns depart from the isolated pattern [3], [4]. An estimator that assumes the ideal steering vector is then biased, and the bias is deterministic, so integration does not remove it [5].

Compensating coupling with a coupling matrix is established [6], [7], and automotive practice relies on measured angular calibration [8], [9]. Recent work estimates coupling jointly with the target parameters [10] or blindly from radar data [11], or includes embedded patterns in the signal model of sparse arrays [12]. In every case, the processor uses an estimate of the coupling, obtained from a reduced model, a full-wave simulation, or a calibration that drifts. How accurate that estimate must be, which of its errors matter most, and how much calibration effort meets a given angular tolerance are questions the literature answers only indirectly.

In this study, we address those questions for one fully specified 77 GHz receive array. The compensation methods themselves are standard; our contribution is the quantitative error analysis around them:

1) We derive a phase-slope model of the beamforming bias for any manifold error and verify it against exact estimates (within 0.004°). The model explains the bias profile and predicts the residual left by an inaccurate coupling matrix.

2) We quantify residual bias against magnitude, phase, entry-wise and model-structure errors of the coupling matrix, across coupling strengths, coupling phases, angles, and SNR, using a reduced banded model and a network-consistent dipole benchmark that separates coupling coefficients from S-parameters.

3) We translate these tolerances into calibration requirements (calibration SNR and number of angles) for diagonal, Toeplitz-structured and unstructured estimators of the array response, and into an error budget with channel phase errors.

4) We embed everything in a consistent FMCW chain with a corrected link budget and report detection, angle and lateral-position errors with confidence intervals, and we release the code.

Section II reviews related work. Section III defines the antenna and radar model, Section IV the estimators and evaluation methods, and Section V the results. Section VI states the limitations and Section VII concludes.

RELATED WORK AND RESEARCH GAP

Automotive arrays. Waldschmidt et al. [1] review the path to today's 77 GHz sensors, and Sun and Zhang [2] describe how imaging ("4D") radar relies on larger MIMO and sparse apertures to improve angular resolution. Recent 77 GHz array designs report measured patterns and study interactions between adjacent subarrays [13]; defected ground and parasitic structures can reduce the coupling itself [14], and the radome must be shaped to preserve wide-angle performance [15].

Coupling models and compensation. Gupta and Ksienski [3] related the received voltages of a coupled array to its impedance matrix, which yields a coupling matrix for given terminations. Steyskal and Herd [6] compensated coupling in small arrays with such a matrix, and Friedlander and Weiss [5] showed that unknown coupling biases direction finding and estimated coupling and angles jointly. Pozar's active element pattern [4] makes clear that real coupling is angle-dependent, which a single matrix only approximates. Lan et al. [10] treat unknown coupling coefficients within adaptive detection and DoA estimation, and Swindlehurst and Kailath [16] established first-order performance analysis under model errors, which our phase-slope model specializes to beamforming.

Calibration in automotive radar. Schmid et al. [7] quantified coupling-induced sidelobes in a 77 GHz FMCW MIMO radar and compensated them in measurement. Vasanelli et al. [8] describe angular calibration with measured responses, and Dürr et al. reduce the calibration effort through phase symmetry [17], modal wave expansion [9], and virtual phase-center analysis for very large arrays [18]. Amani et al. [12] and Goldgraber Casspi et al. [11] include coupling explicitly in single-snapshot DoA and in blind calibration. Table 1 summarizes the relation.

TABLE 1: Representative Work on Coupling and Calibration Compared with this Study.

Work	Coupling or calibration treatment	Evidence	Main metric
[5]	Unknown C, joint estimation	Simulation	DoA error
[7]	Coupling compensation, 77 GHz MIMO	Measurement	Sidelobe level
[8]	Measured angular calibration	Measurement	DoA, field of view
[9]	Model-based calibration (incl. coupling)	Measurement	DoA vs. effort
[12]	Embedded patterns, coupling matrices	Simulation	Single-snapshot DoA
[10]	Unknown coupling coefficients	Analysis, sim.	Detection, DoA
[11]	Blind coupling/gain/phase	Simulation	DoA error
This work	Banded and network models; error and calibration study	Simulation	Bias (analytic + exact), RMSE vs. CRB, lateral error, calibration SNR

Research gap. Existing studies address array calibration and coupling estimation, but the impact of coupling-matrix errors on angular and lateral accuracy, and the calibration effort required to meet specified tolerances, remain insufficiently quantified for automotive arrays. This study investigates these relationships using a consistent 77-GHz design through simulation (Section VI).

ANTENNA AND FMCW RADAR SYSTEM MODEL

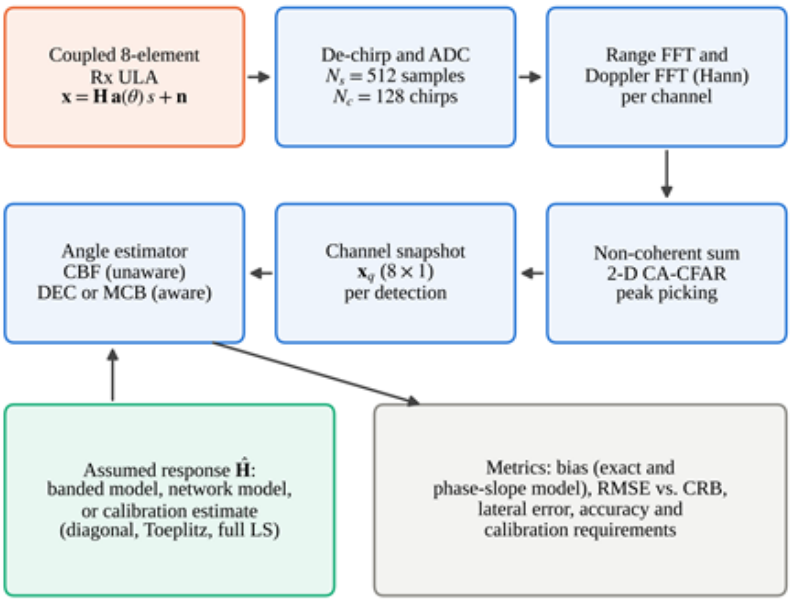


FIGURE 1: Simulation Framework. The Coupled Receive Array Feeds a Complete FMCW Chain; Each CFAR Detection Yields an Eight-Channel Snapshot That a Coupling-Unaware (CBF) or Coupling-Aware (DEC, MCB) Estimator Processes with an Assumed Array Response $\hat{\mathbf{H}}$.

TABLE 2: FMCW Parameters.

Parameter	Symbol	Value
Centre frequency / sweep	f_0 / B	77 GHz / 1 GHz (76.5–77.5 GHz)
Wavelength ($c = 3 \times 10^8$ m/s)	λ_0	3.896 mm
Ramp duration / slope	T_c / S	25.6 µs / 39.06 MHz/µs
Complex sampling / samples	f_s / N_s	20 MHz / 512
Repetition interval / chirps	T_r / N_c	30.0 µs / 128 (frame 3.84 ms)
Range resolution / max. range	ΔR / $R_{\max}$	0.15 m / 76.8 m
Velocity resolution / max.	Δv / $v_{\max}$	0.507 m/s / ±32.47 m/s
Tx / Rx channels	—	1 / 8

A. FMCW Waveform

One transmitter illuminates the scene, and an eight-channel uniform linear array (ULA) receives (SIMO); this isolates receive-side coupling, and Section VI discusses MIMO. Linear up-chirps of bandwidth B and duration T_c have slope

$$S = \frac{B}{T_c}. \tag{1}$$

De-chirping as $s_{\text{tx}} s_{\text{rx}}^*$, a point target at range R with radial velocity v (positive for increasing range) yields

$$f_b = \frac{2SR}{c}, \qquad f_D = \frac{2v}{\lambda_0}, \tag{2}$$

and, with complex sampling at f_s, $N_s = f_s T_c$ samples per chirp, N_c chirps and repetition interval T_r,

$$\Delta R = \frac{c}{2B}, \quad R_{\max} = \frac{c f_s}{2S}, \quad v_{\max} = \frac{\lambda_0}{4T_r}, \quad \Delta v = \frac{\lambda_0}{2N_c T_r}. \tag{3}$$

Table 2 lists the values, all recomputed from (1)–(3); $R_{\max}/N_s = \Delta R$ confirms the consistency of sampling and sweep. A 12 m/s target moves 4.6 cm in one frame and its Doppler term shifts the range by 2.4 cm, both below ΔR.

B. Patch Element and Array

The element is an inset-fed rectangular patch on RO3003 ($\varepsilon_r = 3.00$, $\tan\delta = 0.0010$, $h = 0.127$ mm) [19], designed with the transmission-line model [20]:

$$W = \frac{c}{2f_0}\sqrt{\frac{2}{\varepsilon_r + 1}}, \quad \varepsilon_{\text{eff}} = \frac{\varepsilon_r + 1}{2} + \frac{\varepsilon_r - 1}{2}\left(1 + \frac{12h}{W}\right)^{-1/2}, \tag{4}$$

$$\Delta L = 0.412\,h\,\frac{(\varepsilon_{\text{eff}} + 0.3)(W/h + 0.264)}{(\varepsilon_{\text{eff}} - 0.258)(W/h + 0.8)}, \quad L = \frac{c}{2f_0\sqrt{\varepsilon_{\text{eff}}}} - 2\Delta L. \tag{5}$$

Table 3 summarizes the results: edge resistance (including G_{12}) of 262 Ω, 0.38-mm inset depth for 50 Ω, 6.4-dBi directivity, and 3.5% fractional bandwidth (VSWR ≤ 2).

These first-order estimates require full-wave validation: permittivity (±0.04) and length (±10 µm) variations shift resonance by ∓0.46 and ∓0.65 GHz, respectively. Their combined RSS uncertainty (0.80 GHz) approaches the 0.86-GHz margin and exceeds it in the worst case (1.1 GHz). Moreover, the permittivity specification extends only to 40 GHz [19], while conductor, roughness, and feed losses are omitted. A recent 77-GHz PCB array reports approximately 90% radiation efficiency [13].

TABLE 3: Antenna, Substrate and Array Parameters (Analytical).

Quantity	Value
Patch width W / length L	1.377 mm / 1.065 mm
ε_{eff} / ΔL	2.689 / 0.0614 mm
Edge resistance / inset depth	≈262 Ω / ≈0.38 mm
Directivity (two-slot model)	6.4 dBi
Bandwidth (VSWR ≤ 2)	≈3.5% (2.7 GHz)
Δf_r for $\Delta\varepsilon_r = \pm 0.04$ / $\Delta L = \pm 10$ µm	∓0.46 GHz / ∓0.64–0.65 GHz
Elements / spacing / edge gap	8 / 1.948 mm / 0.571 mm
Aperture $(N-1)d$	13.64 mm ($3.5\lambda_0$)

Figure 2(a) shows the array. For a maximum scan angle $\theta_{\max}$, grating lobes stay out of visible space when [20].

$$\frac{d}{\lambda_0} \le \frac{1}{1+|\sin\theta_{\max}|}, \tag{6}$$

So, a ±60° field of view allows $d \le 0.536\lambda_0$. The half-wavelength spacing is near this limit; coupling must therefore be compensated rather than avoided by spacing.

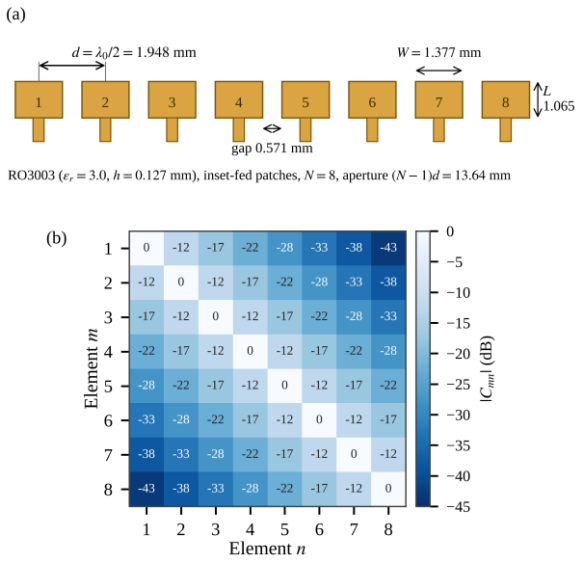


FIGURE 2: (a) Eight-Element $\lambda_0/2$ Patch ULA on RO3003 (Feeds Not to Scale). (b) Magnitude of the Banded Coupling Matrix (8) FOR $\rho = 0.25$, $\gamma = 0.55$, $\varphi = 35°$.

C. Coupled Array Manifold and Coupling Models

With $d = \lambda_0/2$, the ideal steering vector and the received snapshot are

$$\mathrm{a}(\theta) = \left[1,\ e^{j\pi\sin\theta},\ \ldots,\ e^{j\pi(N-1)\sin\theta}\right]^T,$$
$$\mathrm{x} = \mathrm{H}\,\mathrm{a}(\theta)\,s + \mathrm{n}, \tag{7}$$

Where $\mathrm{H} = \Gamma\mathrm{C}$ combines the coupling matrix C with diagonal channel gains Γ (Γ = I unless stated), s is the target amplitude and n white noise of variance σ_n^2 per channel. We use two coupling models.

Reduced banded model. As the baseline, we use the symmetric Toeplitz matrix

$$C_{mn} = \begin{cases} 1, & m = n, \\ \rho\,\gamma^{|m-n|-1} e^{-j\varphi|m-n|}, & m \ne n, \end{cases} \tag{8}$$

With adjacent magnitude $\rho = 0.25$ (−12.0 dB), decay $\gamma = 0.55$ and phase $\varphi = 35°$ (Fig. 2(b)). Its condition number is 2.15 and stays below 7 for $\rho \le 1$. The parameters are assumptions, not extracted values; we therefore sweep them. The model is frequency- and angle-independent and not power-conserving ($\| \mathrm{Ca} \|^2/N$ ranges from +3.4 dB at broadside to −2.6 dB at 60°), so we report only relative quantities.

Network-consistent benchmark. To test whether conclusions depend on the banded parametrization, we also derive C from an impedance matrix Z through the open-circuit-voltage relation [3]

$$\mathrm{C} = (Z_A + Z_L)(\mathrm{Z} + Z_L\mathrm{I})^{-1}, \tag{9}$$

for side-by-side thin half-wavelength dipoles at $\lambda_0/2$ ($Z_A = 73.1 + j42.5$ Ω, induced-EMF mutual impedances [20], $Z_{12} = -12.5 - j29.9$ Ω) and $Z_L = 50$ Ω. This benchmark is not a patch model; it is a passive, reciprocal network whose coupling differs structurally from (8). It also shows that a coupling coefficient is not an S-parameter: the adjacent entry is $|C_{12}| = -13.9$ dB at 38°, whereas $|S_{21}| = -16.2$ dB at −154° ($|S_{11}| = -10.8$ dB, 50 Ω reference). Reading ρ as a measured $|S_{21}|$ is therefore incorrect without the network relation (9) and the port terminations.

D. Data Cube and Link Budget

For target i, the de-chirped sample of channel k, fast-time index n and chirp l is

$$x_k[n,l] = \sum_i \alpha_i\ b_k(\theta_i) \times e^{j2\pi\left[(f_{b,i}+f_{D,i})\frac{n}{f_s}+f_{D,i}\,l\,T_r\right]} + w_k[n,l], \tag{10}$$

With $\mathrm{b}(\theta) = \mathrm{Ha}(\theta)$, random target phases and unit-variance complex noise w_k. Amplitudes follow the radar equation [21].

$$P_r = \frac{P_t G_t G_e \lambda_0^2 \sigma}{(4\pi)^3 R^4 L_s}, \quad (11)$$

With per-sample noise power $kT_0 f_s F$. Table 4 lists the assumptions: the element gain G_e is the 6.4 dBi directivity (an upper bound on realized gain), the transmitter feeds an equal-aperture eight-element sub-array ($G_t = 15.4$ dBi), and $L_s = 6$ dB lumps feed, radome and implementation losses. A 10 m^2 target at 40 m then has a per-channel SNR of 24.2 dB after range–Doppler integration (30.2 dB without L_s). This figure matters for interpretation: Section V shows that above about 15–20 dB the uncompensated angle error is set by bias, not noise.

TABLE 4: Link Budget Per Receive Channel ($R = 40$ m, $\sigma = 10$ m^2).

Term	Value
P_t / G_t / G_e	10 dBm / 15.4 dBi / 6.4 dBi
λ_0^2 / σ / $(4\pi)^{-3}$ / R^{-4}	−48.2 / +10.0 / −33.0 / −64.1 dB
System loss L_s (assumed)	−6.0 dB
P_r / noise $kT_0 f_s F$ ($F = 12$ dB)	−109.4 dBm / −89.0 dBm
SNR per sample	−20.4 dB
Integration $N_s N_c$ / Hann loss	+48.2 dB / −3.5 dB
SNR after integration / after 8-ch. beamforming	24.2 dB / 33.3 dB

Estimation and Evaluation Methodology

A. Detection

Each channel is Hann-windowed and transformed in range and Doppler. Two-dimensional cell averaging CFAR [21] operates on the non-coherent channel sum $P[r,q] = \sum_k |Y_k[r,q]|^2$ with 2 guard and 8 × 4 training cells per side ($M = 248$). With independent cells, $P/(P + \sum_{\text{train}} P) \sim \text{Beta}(N, NM)$ under noise only, so

$$P[r,q] > \frac{\alpha}{M} \sum_{\text{train}} P, \qquad \alpha = \frac{Mt}{1-t}, \quad (12)$$

Where t is the $(1 - P_{\text{fa}})$ quantile; $P_{\text{fa}} = 10^{-6}$ gives $\alpha = 5.6$ dB. Local maxima over 5 × 5 cells are kept, and the eight-channel snapshot $\mathbf{x}_q$ of each detection goes to the angle estimator.

B. Angle Estimators

The coupling-unaware conventional beamformer (CBF), the decoupling estimator (DEC) and the matched coupled-manifold beamformer (MCB) maximize, respectively,

$$P_{\text{CBF}} = \left|\mathrm{a}^H \mathrm{x}_q\right|^2, \quad P_{\text{DEC}} = \left|\mathrm{a}^H \mathrm{T}_\mu \mathrm{x}_q\right|^2, \quad P_{\text{MCB}} = \frac{\left|\hat{\mathrm{b}}^H \mathrm{x}_q\right|^2}{\| \hat{\mathrm{b}} \|^2}, \quad (13)$$

With $\mathrm{T}_\mu = \left(\hat{\mathrm{H}}^H \hat{\mathrm{H}} + \mu \mathrm{I}\right)^{-1} \hat{\mathrm{H}}^H$, $\hat{\mathrm{b}}(\theta) = \hat{\mathrm{H}}\mathrm{a}(\theta)$, and $\hat{\mathrm{H}}$ the response assumed by the processor. DEC applies the regularized least-squares decoupling of the snapshot ($\mu = 0$ gives $\hat{\mathrm{H}}^{-1}$); it is the receive-side form of the weight pre-distortion of [6]. Because these weights have a closed form, heuristic weight optimization is unnecessary. MCB is the maximum-likelihood estimator for a single source and known H. Its normalization by $\| \hat{\mathrm{b}} \|^2$ is essential: without it, the peak moves toward angles where the coupled manifold is strong, and the "compensated" bias doubles (Section V-B).

C. Phase-Slope Model of the Bias

For any snapshot of the form $\mathrm{z} = \mathrm{a}(\theta_0) \odot (1 + \epsilon)$, write $1 + \epsilon_n = A_n e^{j\psi_n}$ and $m_n = n - (N-1)/2$. Expanding $|\mathrm{a}^H(\theta)\mathrm{z}|$ to second order in the residual phase $\psi_n - \pi m_n(\sin\theta - \sin\theta_0)$ shows that CBF fits a straight line to the excess phase by amplitude-weighted least squares (Appendix A), which gives the bias

$$\delta\theta \approx \frac{\sum_n A_n \tilde{m}_n \psi_n}{\pi \cos\theta_0 \sum_n A_n \tilde{m}_n^2}, \qquad \tilde{m}_n = m_n - \frac{\sum_n A_n m_n}{\sum_n A_n}. \quad (14)$$

For small errors, (14) reduces to $\delta\theta \approx \sum_n m_n \operatorname{Im}\epsilon_n / (\pi \cos\theta_0 \sum_n m_n^2)$, a beamforming instance of first-order model-error analysis [16]. The model applies to the uncompensated case with $\epsilon = (\mathrm{Ha}) \oslash \mathrm{a} - 1$ and to DEC with $\epsilon = \left(\mathrm{T}_\mu \mathrm{Ha}\right) \oslash \mathrm{a} - 1$. Two consequences follow. Only the component of the excess phase that is linear across the aperture produces bias, so symmetric perturbations, such as broadside coupling in a symmetric Toeplitz array, cause none. And the residual bias is linear in a small error of $\hat{\mathrm{H}}$ (Appendix B), which explains the linear trends in Section V-E.

D. Calibration-Based Estimation of the Response

To relate accuracy requirements to calibration effort, we simulate a calibration with a reflector at K known angles, uniformly spaced in ±60°, with unknown complex reflector amplitudes s_k and a given SNR per element and angle. The true response includes channel errors (0.5 dB and 10° RMS). We compare four estimates of H : none ($\hat{\mathrm{H}} = \mathrm{I}$); boresight gain and phase only (a diagonal $\hat{\mathrm{H}}$ from the 0° snapshot); diagonal gains times a symmetric Toeplitz coupling matrix; and an unstructured 8 × 8 matrix. The last two are fitted by alternating least squares over $\hat{\mathrm{H}}$ and the s_k (150 iterations, initialized with the boresight estimate). Each calibrated $\hat{\mathrm{H}}$ is scored by the maximum noise-free DEC bias over ±60° (4° steps).

E. Metrics, Statistics and Reproducibility

We report the peak sidelobe level outside the ideal first-null region, the half-power beamwidth, the pointing error, and the processing efficiency $\eta = |\mathrm{w}^H \mathrm{b}|^2 / (\| \mathrm{w} \|^2 \| \mathrm{b} \|^2)$, which compares weights on the same coupled array independently of the scaling of C. For angle estimation, we report the noise-free bias, the RMSE, and the deterministic single-snapshot CRB for known H [22],

$$\mathrm{CRB}(\theta_0) = \frac{\sigma_n^2}{2|s|^2 \; \| \, \mathrm{P}_\mathrm{b}^{\perp} \, \dot{\mathrm{b}}(\theta_0) \, \|^2}, \qquad \Delta y \approx R\cos\theta_0 \, \Delta\theta, \tag{15}$$

Where $\dot{\mathrm{b}} = \partial \mathrm{b} / \partial\theta$ and $\mathrm{P}_\mathrm{b}^{\perp} = \mathrm{I} - \mathrm{b}\mathrm{b}^H / \| \, \mathrm{b} \, \|^2$; Δy converts an angle error into lateral error. Angle spectra

are searched on a 0.02° grid with parabolic interpolation. Monte Carlo sizes are 600 trials per SNR point, 150 random matrices per error level, 200 calibrations per setting, 400 trials per error-budget cell, and 200 independent FMCW frames. We give 95% bootstrap confidence intervals for RMSE values, normal intervals for means, and Wilson intervals for detection probabilities. Each experiment uses its own seeded generator; the Python code (Python 3.13, NumPy 2.5, SciPy 1.18) reproduces all figures and tables in about 4 min on a single CPU core and is provided as supplementary material.

RESULTS AND DISCUSSION

A. Beam-Pattern Distortion

Fig. 3 and Table 5 compare the receive patterns. The ideal eight-element PSLL is −12.8 dB (the often quoted −13.3 dB applies only to a continuous aperture). At broadside, coupling lowers the sidelobes to −14.5 dB and widens the beam from 12.8° to 13.5°: the edge elements have neighbours on one side only, so the effective excitation tapers by 2.4 dB toward the edges, and its symmetric phase curvature (−17° at the edges, −27° at the centre) fills the nulls without steering the beam. Steering makes the perturbation asymmetric. At 40° the PSLL rises by 2.4 dB to −10.4 dB, and the beam points 0.46° short; at 20° it points 0.95° short. The decoupling weights restore the ideal pattern exactly when $\widehat{\mathrm{H}} = \mathrm{H}$, which verifies the implementation but says nothing about robustness (Section V-E). Relative to matched weights, conventional weights lose at most 0.11 dB and decoupling weights at most 0.29 dB.

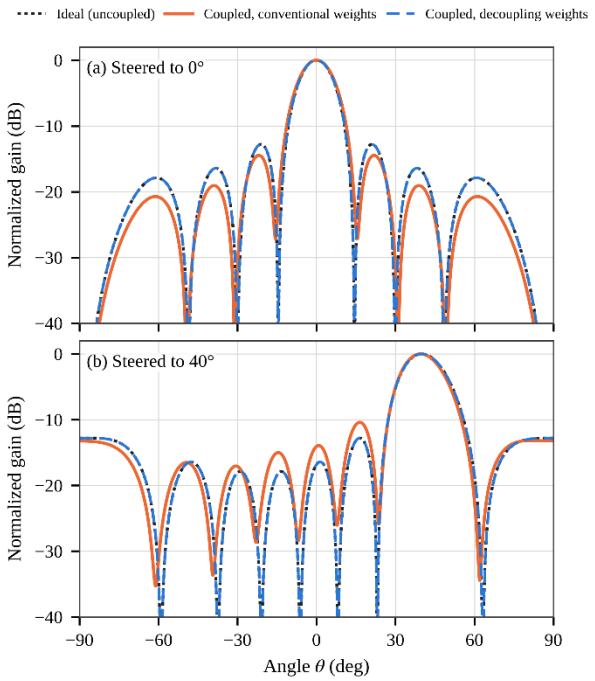


FIGURE 3: Receive Beam Patterns of The Ideal Array and of The Coupled Array with Conventional and Decoupling Weights, Steered to (a) 0° and (b) 40°.

B. Bias Profile and Mechanism

Figure 4(a) shows the noise-free bias. CBF pulls every estimate toward broadside, with −0.09° at 5°, −0.95° at 20°, a maximum of −0.97° at 22°, and −0.20° at 60°; the bias peaks at intermediate angles rather than growing monotonically. The phase-slope model (14) reproduces the exact curve within 0.004° everywhere in ±60°. At 22°, for example, the excess phase falls from +17.0° at element 1 to −10.1° at element 8, and its amplitude-weighted slope opposes the steering phase. The peak location is set by the coupling phase: it moves from 11° (1.38° peak) at $\varphi = 0°$ to 22° (0.97°) at 35°, 32° (0.91°) at 60° and 45° (0.90°) at 90°. Fig. 4(b) shows that the maximum bias grows almost linearly with ρ (0.42° at 0.1, 1.43° at 0.4). Both coupling-aware estimators remove the bias when $\widehat{\mathrm{H}} = \mathrm{H}$ (residual below 10^{-5} degrees). Without the normalization in (13), the coupled-manifold beamformer reaches 1.93°, twice the uncompensated bias.

TABLE 5: Beam Metrics of the Coupled Array (Banded Model).

θ_s	Case	PSLL (dB)	HPBW (°)	Point. err. (°)	η (dB)
0°	Ideal	−12.8	12.8	0.00	—
	Coupled, CBF	−14.5	13.5	0.00	−0.06
	Coupled, DEC	−12.8	12.8	0.00	−0.20
20°	Ideal	−12.8	13.6	0.00	—
	Coupled, CBF	−12.1	13.8	−0.95	−0.11
	Coupled, DEC	−12.8	13.6	0.00	−0.29
40°	Ideal	−12.8	16.9	0.00	—
	Coupled, CBF	−10.4	16.3	−0.46	−0.09
	Coupled, DEC	−12.8	16.9	0.00	−0.17

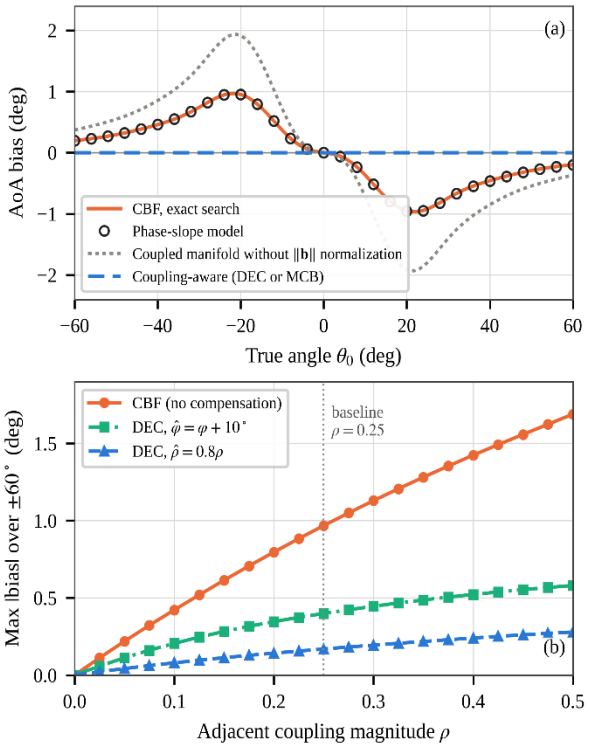


FIGURE 4: (a) Noise-Free AOA Bias Versus True Angle (Banded Model, $\rho = 0.25$): CBF (Exact Search and Phase-Slope Model (14)), Coupled-Manifold Beamformer without Normalization, and Coupling-Aware Estimators. (B) Maximum |Bias| Over ±60° Versus ρ , Uncompensated and with A 20% Magnitude Or 10° Phase Error in $\hat{C}$.

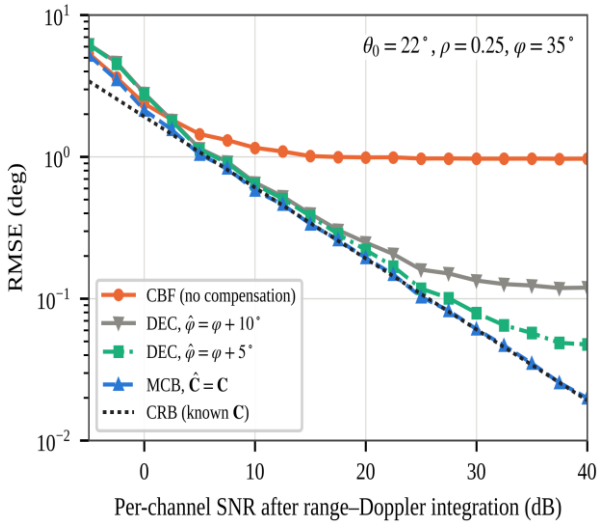


FIGURE 5: RMSE at $\theta_0 = 22°$ Versus Per-Channel SNR After Integration (600 Trials Per Point), for CBF, MCB with Exact C, DEC with a 5° or 10° Error in $\hat{\varphi}$, and the CRB.

C. Noise, the CRB and Mismatch Floors

Figure 5 shows the RMSE at 22°. Below about 0 dB, all estimators enter the threshold region. Above about 5 dB, MCB follows the CRB (0.194° against 0.192° at 20 dB; 0.061° against 0.061° at 30 dB), and DEC (not shown) stays 6–13% above MCB because decoupling colours the noise: the decoupled noise has covariance $\sigma_n^2 T_\mu T_\mu^H$, so its mean power per channel rises by the factor $\mathrm{tr}(T_\mu T_\mu^H)/N$. For $\mu = 0$, this factor is 0.75 dB at $\rho = 0.25$ (2.6 dB at $\rho = 0.5$). CBF levels off at its 0.97° bias above about 15–20 dB (0.37° at 45°). An inexact matrix creates its own floor: with $\hat{\varphi} = \varphi + 5°$ the RMSE stops near 0.05°, and with +10° near 0.12° at 22°. The 95% bootstrap intervals of all RMSE points lie within ±11% of the values. Because Table 4 places vehicle-sized targets above 20 dB, the deployed accuracy is governed by bias and by the accuracy of $\hat{H}$, not by noise.

D. End-to-End FMCW Scenario

We simulate four targets with the budget of Table 4: T1 at 12.0 m, −8 m/s, −35° (10 m^2); T2 at 28.5 m, +12 m/s, +22° (10 m^2); T3 at 41.0 m, 0 m/s, +8° (10 m^2); and T4 at 58.0 m, +4 m/s, −12° (1 m^2). Fig. 6 shows one frame. Over 200 frames, CFAR detected every target in every frame (Wilson 95% lower bound 0.98) with 16 false alarms (1.2×10^{-6} per cell, near the design value), and median range and velocity estimates fall within one cell of the truth.

TABLE 6: End-To-End Angle Errors Over 200 Frames ($\hat{H} = H$).

Quantity	T1	T2	T3	T4
Range (m) / angle (°)	12.0 / −35	28.5 / +22	41.0 / +8	58.0 / −12
SNR (dB)	45.1	30.1	23.8	7.8
CBF mean error (°)	+0.573	−0.970	−0.229	+0.516
CBF std. dev. (°)	0.016	0.071	0.094	0.701
DEC RMSE (°)	0.016	0.074	0.103	0.776
MCB RMSE (°)	0.015	0.069	0.098	0.739
MCB 95% CI (°)	0.014 −0.016	0.062 −0.076	0.088 −0.108	0.662 −0.819
CRB (°)	0.014	0.060	0.101	0.677
Δy CBF (cm)	9.8	44.9	17.6	86.1
Δy MCB (cm)	0.3	3.2	6.9	73.2

SNR per channel after integration; Δy is the lateral RMSE from (15).

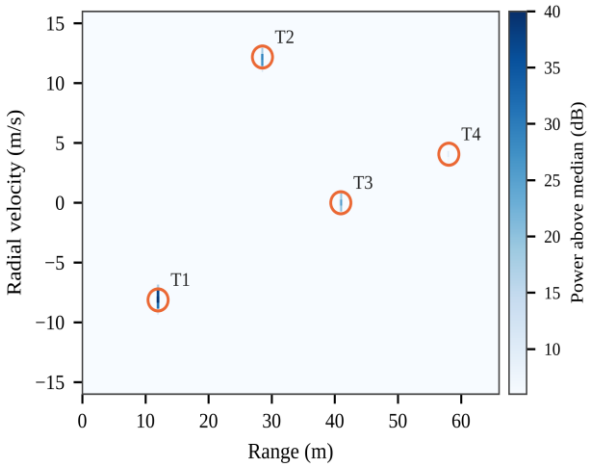


FIGURE 6: Range–Doppler MAP (Non-Coherent Sum Over Eight Channels) of One Simulated Frame; Circles Mark CA-CFAR Detections ($P_{fa} = 10^{-6}$). Display Cropped to 0–66 m and ±16 m/s.

Table 6 lists the angle errors. The mean CBF error agrees with the noise-free bias to within 0.006° for every target. For T2, CBF misplaces the target by 0.97° (0.45 m laterally at 28.5 m); MCB reduces the RMSE to 0.069° (3.2 cm), close to the 0.060° CRB. At 12 m, T1 still shifts by 9.8 cm. T4 (7.8 dB) is noise-limited: compensation removes its 0.52° mean bias, but the RMSE falls only from 0.87° to 0.74° because the CRB is 0.68°. Bias, not noise, dominates the uncompensated error of the three vehicle-sized targets.

E. Sensitivity to Coupling-Matrix Errors

Fig. 7 examines the sensitivity to imperfect coupling-matrix knowledge. For the baseline, residual maximum bias increases linearly with magnitude erro (0.08° per 10%, reaching 0.44° at −50%) and phase error (0.21° at ±5°, 0.40–0.42° at ±10%, and 0.76–0.80° at ±20% for DEC). Beyond +27° or −26°, compensation performs worse than no compensation. DEC and MCB exhibit similar behavior, while the phase-slope model predicts both curves within 0.2% for errors up to ±20%.

For independent complex errors across all off-diagonal entries, with relative standard deviation [value missing in the supplied text], the mean residual bias reaches 0.11°, 0.22°, and 0.43% at 5%, 10%, and 20% error, respectively. The 95th percentile exceeds the uncompensated bias at approximately 24% error. A 10% complex entry error corresponds to RMS magnitude and phase errors of approximately 0.6 dB and 4°, respectively. Table 7 further examines whether the identified error thresholds remain valid across configurations beyond the baseline case. A 20% magnitude error retains only 9–19% of the original bias across all nine evaluated cases, indicating consistent compensation performance under magnitude perturbations. However, the sensitivity to a 10° phase error depends strongly on the actual coupling phase. For real coupling (0°), the residual bias remains relatively low at 10–11%, whereas coupling phases of 35° and 90° produce substantially higher residuals of 39–51%. The crossover phase error also varies considerably, ranging from 20° to 42° across the evaluated cases. These findings indicate that phase accuracy is generally more critical than magnitude accuracy for complex coupling coefficients, which are representative of practical coupling conditions (Section V-G). Nevertheless, this relationship is not universal and depends on the underlying coupling phase. Furthermore, because both the original and residual biases scale with coupling magnitude, the corresponding relative error tolerances remain nearly independent of coupling strength.

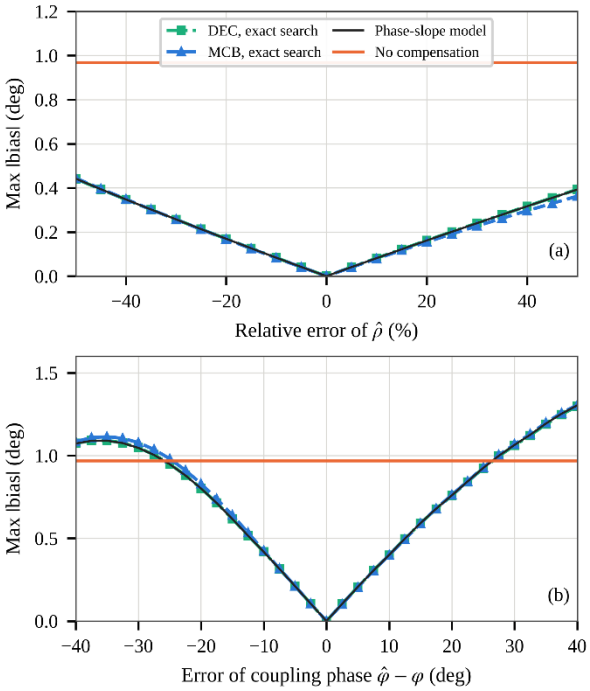


FIGURE 7: Maximum Residual |Bias| Over ±60° with a Mismatched Banded Matrix: (a) Error in $\hat{\rho}$; (b) Error in $\hat{\varphi}$. Lines: Phase-Slope Model; Horizontal Line: Uncompensated Bias (0.97°).

F. Calibration Requirements

Fig. 8(a) evaluates post-calibration bias under channel errors across different angles. Without calibration, combined channel and coupling errors produce a 95th-percentile bias of approximately 2°. Boresight calibration removes channel errors but retains angle-dependent coupling bias (0.95°). Full-response estimators approach zero bias, with the Toeplitz model reaching below 0.2° at 31 dB calibration SNR (0.1° at 37 dB), compared with 34.6 dB (41.7 dB for 0.1°) for the unstructured model. This improvement reflects the reduced parameter count: 30 versus 128 real unknowns, saving 3.5–4.8 dB of calibration SNR (2.2–3× averaging).

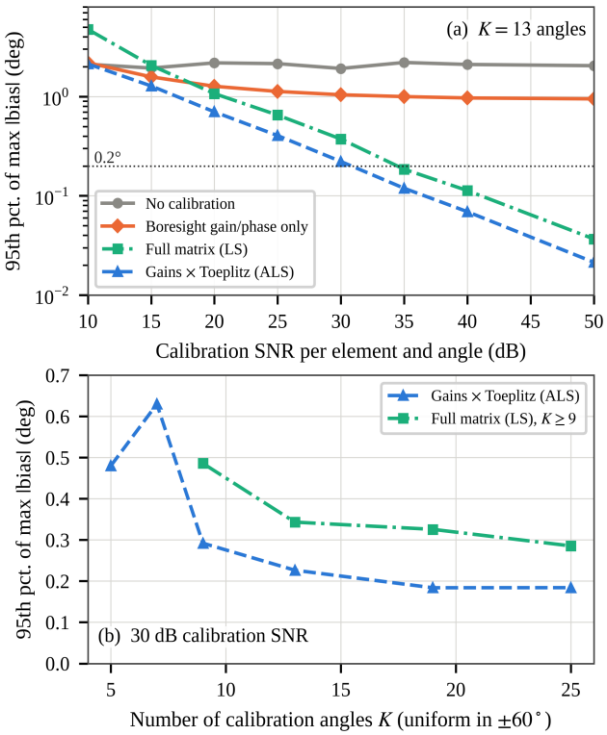


FIGURE 8: 95th Percentile of the Maximum Residual Bias After Calibration (200 Trials Per Point; Channel Errors 0.5 Db / 10° Rms): (A) Versus Calibration Snr For $K = 13$; (B) Versus the Number of Calibration Angles at 30 dB.

Figure 8(b) shows that more angles help at 30 dB, lowering the 95th percentile from 0.29° (image) to 0.18° (image) for the Toeplitz model, but not monotonically: image (0.63°) is worse than image (0.48°) for these uniformly spaced angles, so the angle placement matters, and we did not optimize it. Regularization is a secondary lever here because the matrices are well conditioned. For 40 unstructured estimates calibrated at 20 dB SNR, image lowered the mean residual bias from 0.64° to 0.55° (paired difference 0.09°, 95% CI 0.06–0.13°) and left the RMSE at 22°- and 20-dB operating SNR unchanged (0.31° and 0.32°), whereas image raised that RMSE to 0.46°.

TABLE 7: Robustness of The Accuracy Thresholds (Banded Model, Maximum Over ±60°).

ρ	φ	No comp. (°)	10° phase err.	20% magn. err.	Crossover (°)
0.10	0°	0.65	11%	17%	38
0.10	35°	0.42	51%	19%	20
0.10	90°	0.42	51%	18%	20
0.25	0°	1.38	10%	15%	41
0.25	35°	0.97	43%	17%	26
0.25	90°	0.90	47%	14%	22
0.40	0°	1.93	10%	17%	42
0.40	35°	1.43	39%	17%	30
0.40	90°	1.18	43%	9%	23

Percentages give the residual as a fraction of the uncompensated bias (worse sign of the error). Crossover: smallest phase error at which compensation is worse than none.

G. Model-Structure Test with the Network-Consistent Benchmark

Fig. 9 reproduces the key experiments using the dipole coupling model (9) to assess whether the previous findings remain valid under a different coupling structure. Unlike model (8), its lag-2 coefficient (−22.6 dB at −156°) violates the phase progression assumed by the banded model. Consequently, the uncompensated bias increases toward the field-of-view boundaries, reaching 2.23° at ±60°. The optimal three-parameter banded fit (image, image, image) provides only marginal improvement, reducing the bias to 1.99°. In contrast, the optimal symmetric Toeplitz fit reduces it to 0.15°. The remaining error primarily results from edge effects, which introduce slight deviations from the Toeplitz structure in the network matrix.

Errors in mutual impedances again produce residuals that vary approximately linearly with the estimation error. However, unlike the previous coupling model, phase and magnitude errors exhibit comparable effects, producing residual biases of 0.20–0.24° and 0.21–0.22°, respectively, for ±10% errors. No crossover occurs within the investigated ±40° range. These results support two model-independent conclusions: residual bias scales with the relative complex error in the coupling description, and an oversimplified coupling structure can preserve nearly the entire original bias despite optimal parameter fitting. Nevertheless, the detailed bias distribution, peak-error angle, and relative sensitivity to phase and magnitude errors remain dependent on the underlying coupling model.

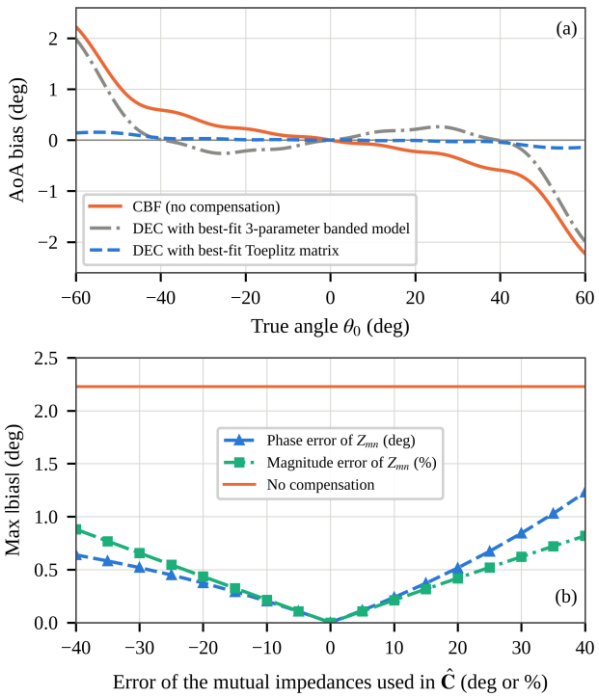


FIGURE 9: Network-consistent dipole benchmark: (a) bias of CBF and of DEC with the best-fit banded and Toeplitz models; (b) residual bias versus phase or magnitude error of the mutual impedances used to build $\hat{\mathbf{C}}$.

TABLE 8: RMS Angle Error (°) Over ±60° for Combined Error Sources.

Coupling-phase error	Channel 0°	2°	5°	10°
0°	0.00	0.13	0.33	0.65
5°	0.09	0.15	0.32	0.69
10°	0.18	0.23	0.36	0.66

H. Channel Phase Errors and Error Budget

Channel phase errors are not part of **C**, so coupling compensation does not remove them. An RMS phase error of 10° raises the mean PSLL of the compensated beam from −12.8 dB to −12.0 dB at broadside and −10.9 dB at 40° (95th percentile −8.8 dB). Table 8 combines both error sources over random angles in ±60°. Channel errors of 2°, 5° and 10° cause 0.13°, 0.33° and 0.65° RMS, and coupling-phase errors of 5° and 10° cause 0.09° and 0.18° RMS; combined, they add approximately in quadrature (within about 5%, comparable to the Monte Carlo spread). For this array, a coupling-phase error of 10° costs about as much as a channel phase error of 3°, so channel calibration remains the first priority and coupling compensation the second.

LIMITATIONS AND ENGINEERING IMPLICATIONS

Implications. For a 77 GHz half-wavelength receive array, (6) leaves little room to reduce coupling by spacing, and the link budget places vehicle-sized targets in the bias-limited regime, so uncompensated coupling sets the angular error floor (about 1° for −12 dB adjacent coupling). Compensation recovers this accuracy at negligible SNR cost, but only with an adequate response model. For a residual near 0.2°, about one fifth of the uncompensated bias, the results suggest three practical targets: a coupling description whose relative complex error stays near 10% or below (phase errors near 5° when the coupling phase is large); a model structure at least as rich as a free-lag Toeplitz matrix, rather than a few-parameter decay law; and calibration at roughly 30–35 dB SNR per element and angle with 9–19 angles. Channel calibration to a few degrees comes first.

Limitations. Table 9 summarizes what the results rest on. Both coupling models are reduced: the banded parameters are assumed, the dipole benchmark is not a patch array, and neither represents angle-dependent embedded patterns [4], surface waves or the radome, which can reshape patterns substantially [15]. The patch design is analytical, with no full-wave verification, fabrication or measurement. The array is a single-transmitter ULA; time-division MIMO adds transmit-side coupling, Doppler-induced phase between transmit slots and a smaller unambiguous velocity [2]. Targets are point scatterers, the chirp is ideal, and the link budget is first order. None of the reported numbers is a measured performance figure.

TABLE 9: Summary of Quantitative Findings and Their Scope.

Finding	Value	Rests on
Uncompensated max. bias	0.97° (2.23° benchmark)	Assumed coupling models
Phase-slope model accuracy	≤ 0.004°	Exact estimator search
SNR cost of compensation	≤ 0.3 dB	Known H
Residual vs. 20% magn. / 10° phase error	9–19% / 10–51%	Banded model, 9 cases
Best-fit banded vs. Toeplitz on benchmark	1.99° vs. 0.15°	Dipole network model
Calibration SNR for 0.2° (Toeplitz / full)	31 / 35 dB	$K = 13$, channel errors 0.5 dB / 10°
Lateral error T2, CBF vs. MCB	44.9 vs. 3.2 cm	Link budget of Table 4

Evidence needed. Three steps would turn this analysis into a validated design: a full-wave model of the array (e.g., CST or HFSS) to extract S, the embedded patterns and an angle-dependent C, and to rerun the supplied scripts with it; a fabricated array with chamber calibration to measure the coupling phase and its board-to-board spread; and recorded radar data, including a MIMO configuration, to confirm the predicted residuals and calibration requirements.

CONCLUSION

In this study, we quantified how the accuracy of the coupling description limits angle estimation in a 77 GHz automotive FMCW radar with an eight-element half-wavelength receive array. We showed that the beamforming bias equals the amplitude-weighted least-squares slope of the excess element phase, a model that matched exact estimates within 0.004° and predicted the residual of inexact compensation within 0.2%. Uncompensated coupling of −12 dB biased angles by up to 0.97°, or 0.45 m at 28.5 m, and dominated the error at the SNRs typical of vehicle targets. Exact compensation removed the bias at under 0.3 dB SNR cost. Inexact compensation left a residual linear in the coupling error: a 20% magnitude error left 9–19% of the bias in all cases, whereas a 10° phase error left 10–51%, the larger values occurring for strongly complex coupling coefficients. A network-consistent benchmark showed that model structure can matter more than parameter accuracy. Toeplitz-structured calibration met a 0.2° tolerance at about 31 dB calibration SNR, 3.5 dB less than an unstructured estimate. These conclusions rest on reduced coupling models and simulation; full-wave extraction, measured calibration and MIMO extensions are the next steps.

Appendix

A. Derivation of the Phase-Slope Model

To derive (14), we write the snapshot of Section IV-C as $z_n = a_n(\theta_0)A_n e^{j\psi_n}$ and set $u = \sin\theta - \sin\theta_0$. Apart from a phase factor that does not change its magnitude,

$$\mathbf{a}^H(\theta)\mathbf{z} = \sum_n A_n\, e^{j\chi_n},$$
$$\chi_n = \psi_n - \pi m_n u. \qquad \text{(A1)}$$

Let $\bar{\chi}$ be the A_n-weighted mean of χ_n and $\xi_n = \chi_n - \bar{\chi}$, so that $\sum_n A_n\, \xi_n = 0$. Expanding $e^{j\xi_n}$ to second order then cancels the first-order term and gives

$$|\mathbf{a}^H(\theta)\mathbf{z}| \approx \sum A_n - \frac{1}{2}\sum A_n\, \xi_n^2. \qquad \text{(A2)}$$

The beamformer therefore selects the u that minimizes $\sum_n A_n\, \xi_n^2$. This is the amplitude-weighted least-squares fit of a straight line with slope πu to ψ_n over m_n, and its normal equation gives

$$\pi u = \frac{\sum_n A_n\, \tilde{m}_n \psi_n}{\sum_n A_n\, \tilde{m}_n^2}, \qquad \text{(A3)}$$

Where the weighted centring in $\tilde{m}_n$ absorbs the intercept $\bar{\chi}$. With $u \approx \cos\theta_0\, \delta\theta$, (A3) becomes (14). When $|\epsilon_n| \ll 1$, $A_n \approx 1$ and $\psi_n \approx Im\, \epsilon_n$, so (14) reduces to the small-error form given in Section IV-C.

B. First-Order Residual of Inexact Compensation

For DEC with $\mu = 0$ and an assumed response $\widehat{\mathrm{H}} = \mathrm{H} + \Delta\mathrm{H}$, the noise-free decoupled snapshot is $\widehat{\mathrm{H}}^{-1}\mathrm{H}\mathrm{a}(\theta_0)s$. For a small $\Delta\mathrm{H}$, $\widehat{\mathrm{H}}^{-1}\mathrm{H} \approx \mathrm{I} - \mathrm{H}^{-1}\Delta\mathrm{H}$, so the excess term of Section IV-C becomes

$$\epsilon \approx -\mathrm{g} \oslash \mathrm{a}(\theta_0), \qquad \mathrm{g} = \mathrm{H}^{-1}\Delta\mathrm{H}\,\mathrm{a}(\theta_0), \qquad \text{(A4)}$$

and the small-error form of (14) gives the residual bias

$$\delta\theta \approx -\frac{\sum_n m_n\; Im\big(g_n/a_n(\theta_0)\big)}{\pi\cos\theta_0 \sum_n m_n^2}. \qquad \text{(A5)}$$

The residual is therefore linear in $\Delta\mathrm{H}$. With $\Gamma = \mathrm{I}$, $\Delta\mathrm{H} = \Delta\mathrm{C}$. For the banded model (8), a relative error κ in $\hat{\rho}$ gives $\Delta\mathrm{C} = \kappa(\mathrm{C} - \mathrm{I})$ exactly, and a small error $\Delta\varphi$ in $\hat{\varphi}$ gives $\Delta C_{mn} \approx -j\Delta\varphi|m - n|C_{mn}$ for $m \neq n$. Both errors enter (A5) linearly, which explains the linear trends of Fig. 7. For the baseline, the maximum of (A5) over ±60° agrees with the exact search within 0.005° for magnitude errors of ±20% and phase errors of ±10°.

ACKNOWLEDGMENT

The authors thank the School of Electronics and Information Engineering and the School of Computer Science and Technology, Nanjing University of Information Science and Technology, for providing research facilities and academic support during this work.

REFERENCES

[1] C. Waldschmidt, J. Hasch, and W. Menzel, "Automotive radar-From first efforts to future systems," *IEEE J. Microw.*, vol. 1, no. 1, pp. 135–148, Jan. 2021, doi: 10.1109/JMW.2020.3033616.

[2] S. Sun and Y. D. Zhang, "4D automotive radar sensing for autonomous vehicles: A sparsity-oriented approach," *IEEE J. Sel. Topics Signal Process.*, vol. 15, no. 4, pp. 879–891, Jun. 2021, doi: 10.1109/JSTSP.2021.3079626.

[3] I. J. Gupta and A. A. Ksienski, "Effect of mutual coupling on the performance of adaptive arrays," *IEEE Trans. Antennas Propag.*, vol. AP-31, no. 5, pp. 785–791, Sep. 1983, doi: 10.1109/TAP.1983.1143128.

[4] D. M. Pozar, "The active element pattern," *IEEE Trans. Antennas Propag.*, vol. 42, no. 8, pp. 1176–1178, Aug. 1994, doi: 10.1109/8.310010.

[5] B. Friedlander and A. J. Weiss, "Direction finding in the presence of mutual coupling," *IEEE Trans. Antennas Propag.*, vol. 39, no. 3, pp. 273–284, Mar. 1991, doi: 10.1109/8.76322.

[6] H. Steyskal and J. S. Herd, "Mutual coupling compensation in small array antennas," *IEEE Trans. Antennas Propag.*, vol. 38, no. 12, pp. 1971–1975, Dec. 1990, doi: 10.1109/8.60990.

[7] C. Schmid, R. Feger, C. Wagner, and A. Stelzer, "Mutual coupling and compensation in FMCW MIMO radar systems," *Frequenz*, vol. 65, no. 9–10, pp. 297–302, 2011, doi: 10.1515/FREQ.2011.044.

[8] C. Vasanelli, F. Roos, A. Dürr, J. Schlichenmaier, P. Hügler, B. Meinecke, M. Steiner, and C. Waldschmidt, "Calibration and direction-of-arrival estimation of millimeter-wave radars: A practical introduction," *IEEE Antennas Propag. Mag.*, vol. 62, no. 6, pp. 34–45, Dec. 2020, doi: 10.1109/MAP.2020.2988528.

[9] A. Dürr, M. Linder, D. Schwarz, and C. Waldschmidt, "Highly efficient angular array calibration based on the modal wave expansion technique," *IEEE Open J. Antennas Propag.*, vol. 2, pp. 938–948, 2021, doi: 10.1109/OJAP.2021.3111447.

[10] L. Lan, M. Rosamilia, A. Aubry, A. De Maio, and G. Liao, "Adaptive target detection and DOA estimation with uniform rectangular arrays in the presence of unknown mutual coupling," *IEEE Trans. Radar Syst.*, vol. 1, pp. 325–338, 2023, doi: 10.1109/TRS.2023.3289991.

[11] S. Goldgraber Casspi, J. Tabrikian, and H. Messer, "Blind array calibration of mutual coupling, phase, and gain for automotive radar," *IEEE Trans. Aerosp. Electron. Syst.*, vol. 60, no. 1, pp. 1060–1073, Feb. 2024, doi: 10.1109/TAES.2023.3336298.

[12] N. Amani, F. Jansen, A. Filippi, M. Ivashina, and R. Maaskant, "Sparse automotive MIMO radar for super-resolution single snapshot DOA estimation with mutual coupling," *IEEE Access*, vol. 9, pp. 146822–146829, 2021, doi: 10.1109/ACCESS.2021.3122967.

[13] D. Bu and S.-W. Qu, "Magneto-electric dipole antenna array for 77 GHz automotive radar," *IET Microw. Antennas Propag.*, vol. 18, no. 2, pp. 96–105, Feb. 2024, doi: 10.1049/mia2.12445.

[14] A. Kumar, A. Q. Ansari, B. K. Kanaujia, J. Kishor, and L. Matekovits, "A review on different techniques of mutual coupling reduction between elements of any MIMO antenna. Part 1: DGSs and parasitic structures," *Radio Sci.*, vol. 56, no. 3, Art. no. e2020RS007122, 2021, doi: 10.1029/2020RS007122.

[15] C. van de Ven, A. Haddadi, and A. Alayón Glazunov, "Shaped radome for wide-angle mmWave automotive RADAR," in *Proc. Int. Symp. Antennas Propag. (ISAP)*, Kuala Lumpur, Malaysia, 2023, doi: 10.1109/ISAP57493.2023.10388563.

[16] A. L. Swindlehurst and T. Kailath, "A performance analysis of subspace-based methods in the presence of model errors, Part I: The MUSIC algorithm," *IEEE Trans. Signal Process.*, vol. 40, no. 7, pp. 1758–1774, Jul. 1992, doi: 10.1109/78.143447.

[17] A. Dürr, M. Linder, and C. Waldschmidt, "Increasing the efficiency and robustness of angular radar calibration by exploiting phase symmetry," in Proc. 17th Eur. Radar Conf. (EuRAD), Utrecht, The Netherlands (online), Jan. 2021, pp. 30–33, doi: 10.1109/EuRAD48048.2021.00019.

[18] A. Dürr, M. Linder, D. Schwarz, T. Frey, and C. Waldschmidt, "Efficient calibration of very large mm-wave radars by virtual phase center analysis," in Proc. 18th Eur. Radar Conf. (EuRAD), London, U.K., Apr. 2022, pp. 521–524, doi: 10.23919/EuRAD50154.2022.9784483.

[19] Rogers Corporation, "RO3000® series circuit materials: RO3003™, RO3006™, RO3010™ and RO3035™ high frequency laminates," data sheet, publication no. 92-130, Chandler, AZ, USA (accessed Oct. 2026).

[20] C. A. Balanis, Antenna Theory: Analysis and Design, 4th ed. Hoboken, NJ, USA: Wiley, 2016.

[21] M. A. Richards, Fundamentals of Radar Signal Processing, 2nd ed. New York, NY, USA: McGraw-Hill, 2014.

[22] P. Stoica and A. Nehorai, "MUSIC, maximum likelihood, and Cramér–Rao bound," IEEE Trans. Acoust., Speech, Signal Process., vol. 37, no. 5, pp. 720–741, May 1989, doi: 10.1109/29.17564.